Terahertz response of microfluidic-jetted three-dimensional flexible metamaterials

Yew Li Hor,[1,*] Zsolt Szabó,[1] Hee C. Lim,[2] John F. Federici,[2] and Er Ping Li[1]

[1]Institute of High Performance Computing, 1 Fusionopolis Way, Singapore 138632

[2]Department of Physics, New Jersey Institute of Technology, Newark, New Jersey 07102, USA

*Corresponding author: ylh3@njit.edu

Received 11 September 2009; revised 10 January 2010; accepted 12 January 2010; posted 19 January 2010 (Doc. ID 117005); published 1 March 2010

We demonstrate the fabrication and characterization of three-dimensional (3D) metamaterials in the terahertz (THz) range using the microfluidic-jetted technique. This technique has proven a convenient technique to fabricate metamaterial structures at the micrometer scale. The metamaterials are fabricated using dodecanethiol functionalized gold nanoparticles on flexible polyimide substrates. The metamaterials consist of alternate layers of single split-ring resonator and microstrip arrays that are stacked to form a 3D metamaterial medium. The fabricated metamaterials, with lattice sizes of 180 μm, are characterized using THz time-domain spectroscopy within 0.1 to 2 THz in the transmission mode. Numerical simulation is performed to calculate the effective metamaterials parameter.

OCIS codes: 160.3918, 220.4000, 300.6495.

1. Introduction

Metamaterials are artificial materials that present extraordinary electromagnetic properties that cannot be achieved in natural materials. Metamaterial research has formed a new field of science and engineering that has evolved at a rapid pace in the past few years. Most of the experiments on metamaterials have been performed at microwave frequencies due to the simplicity of fabrication, as well as the ease of transmission and reflection measurements. There is a sustained effort to push the operation frequency of metamaterials toward the terahertz (THz) frequency region. Metamaterials in THz frequency have been introduced by Yen *et al.* [1] via a two-dimensional layer of split-ring resonator and microstrips with an element size of 50 μm on quartz substrate. Other metamaterials that exhibit electro and magnetic response in the THz region have been described [2–4]. These structures are fabricated using conventional or advanced clean-room MEMS technology.

In this paper, a novel fabrication technique, namely microfluidic jetting, is demonstrated for three-dimensional (3D) conventional design of metamaterial structures in the THz region. This technique originates from ink-jetted printing techniques [5], which have been used as precision deposition tools in a variety of manufacturing processes, such as liquid-crystal displays [6] and organic light emitting diodes [7]. The main difference between ink-jet printing and microfluidic-jetted printing is the size of the nozzles used. Ink-jet fabrication techniques offer economic advantages in situations where the deposited material is expensive. The elimination of dies or photomasks in this technique consequently reduces the fabrication cost and time. In addition, the microfludic-jetted technique is a noncontact fabrication method that minimizes contamination of the fabricated layers. The fabricated metamaterials are characterized in the transmission mode from 0.1 to 2 THz using THz time-domain spectroscopy (THz-TDS). The THz signal only responds to the conductive structure, and the 52 μm thick polyimide film, which is fairly transparent between 0.1 and 1 THz, provides a flexible substrate for the metamaterials.

0003-6935/10/081179-06$15.00/0

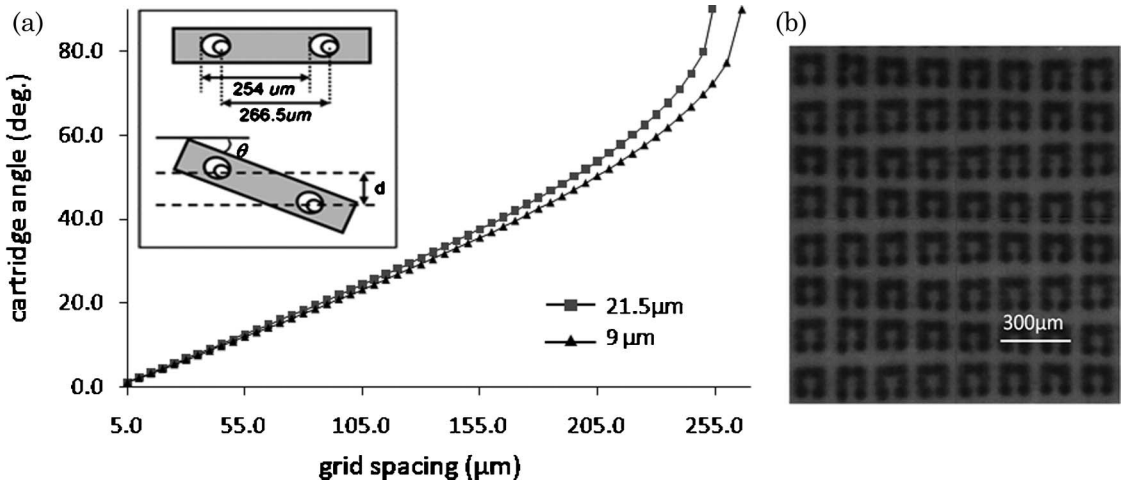

Fig. 1. (a) Calculated cartridge setting angle versus deposited drop spacing for 21.5 and 9 μm nozzle sizes. The inset is the diagram of the nozzles; large and small circles indicate 21.5 μm nozzles and 9 μm nozzles with 254 μm spacing and 266.5 μm spacing, respectively. (b) Image of the SRR structure deposited with an imprecise angle setting used.

2. Microfluidic-Jetted Fabrication

The periodic array of split-ring resonators (SRRs) and microstrips was created on a flexible polyimide substrate using the microfluidic-jetted technique. The microfluidic involved in the fabrication was toluene based, with a 2–4 nm particle size of dodecanethiol functionalized gold nanoparticles (DDT-AuNPs) [8–10] purchased from Sigma-Aldrich. A Dimatix Materials deposition system was used as the primary fabrication tool. However, here in the microfluidic-jetted technique, a 9 μm print head was used instead of the typical 21.5 μm print head. This 9 μm print head consists of 16 nozzles with individual nozzles of diameter 9 μm, which provides microdroplets of 1 pl drop volume. These microdroplets are placed drop by drop on the polyimide substrate to form the desired pattern.

Reduction in drop size is a major consideration in improving the resolution or precision of the microfluidic-jetted technique. Thus, quality control and troubleshooting, such as drop placement accuracy, alignment, and overall jetting uniformity, must be studied to improve quality and to allow the technology to expand into high-resolution THz metamaterial fabrication. The details of the fabrication process can be found in Ref. [11].

In the deposition system, the cartridge angle versus grid spacing was calibrated by the manufacturer based on a 21 μm print head. The cartridge angle, $\theta = \cos^{-1}(d/S_N)$, is the angle adjusted to get precise droplet placement, whereas the grid spacing, d, is the minimum spacing between two droplets and S_N is the nozzle spacing. The inset diagram of Fig. 1(a) illustrates the nozzles of 21.5 (larger circle) and 9 μm (smaller circle) diameters, where the spacing between the 21.5 μm nozzles is 254 μm. For the 9 μm nozzles, the spacing is 266.5 μm. When the cartridge is tilted, the nozzles are also tilted by the same amount because they are parallel to each other. To switch from a 21.5 μm print head to a 9 μm print head, the angle of the deposition cartridge needs to be recalibrated because of different S_N. Figure 1(a) shows a plot of cartridge angle setting versus grid spacing for the 21.5 and 9 μm nozzles. Careful alignment of the cartridge angle is required for micrometer-size structure deposition. Figure 1(b) shows an image of a deposited structure for which an incorrect angle of approximately $\pm 1°$ deviation was used.

The distance between the nozzles and substrate (print height), which is varied from 0.25 to 1.5 mm, is a factor that affects the deposited drop size. Figure 2 shows the drop size versus the printed height deposited at ambient temperature using a 21.5 μm nozzle print head. The curve is saturated at a 1 mm print height, for which the maximum drop size is 58 μm after the sample dries. It is not possible to jet the fluidic below 0.4 mm print height because the nozzle tends to contact the substrate. For samples described in this paper, a print height of 0.5 to 0.6 mm is used.

During fabrication, the jetting performance of the nozzle is controlled by the voltage and force duration, in terms of square waveform, applied to the print

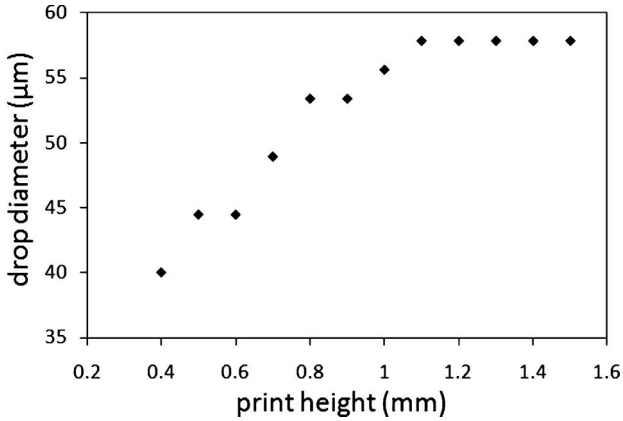

Fig. 2. Drop diameter versus distance between nozzle and substrate.

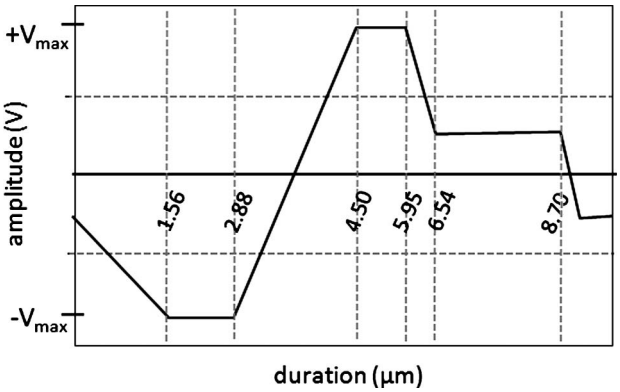

Fig. 3. Waveform setting of DDT-AuNPs solution. V_{max} for DDT-AuNPs was 15–17 V.

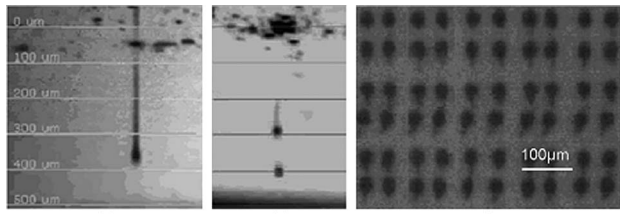

Fig. 4. Image taken by the built-in camera of the deposition system shows the droplet with (a) a perfect drop and (b) a split droplet due to the incorrect waveform setting. (c) Image of the deposition resulting from the split droplet, in which a secondary small dot is formed next to the main drop.

head silicon piezo diaphragm [12]. The square waveforms drive the piezoelectric transducer, which generates pressure to eject the single droplets. The waveform setting is divided into four phases. Phase 1 is the beginning of the firing action, where the fluidic is pulled into the reservoir through the inlet. Phase 2 is a drop ejection phase, where the reservoir is compressed and pressure is generated to eject a drop. Phase 3 is the recovery phase, where the piezo voltage is brought back down and the reservoir decompresses, partially refilling in preparation for the next pulse. In Phase 4, the diaphragm goes back to its natural or relaxing position. Each segment has three properties: duration, amplitude, and slew rate. The applied voltage and slew rate are related to how far and how fast the silicon piezo-diaphragm is bent. The duration controls how long the silicon piezo-diaphragm is maintained in that position. The voltage and the first two phases have the most impact on the jetting process. Changing the properties in these two phases significantly affects drop formation. Figure 3 shows the waveform setting of the DDT-AuNPs solution. Figure 4 shows the jetting satellite droplet with correct and incorrect waveforms, and the image of the structure deposited from the incorrect satellite droplets. An *in situ* "frozen" image of the droplet is shown in Fig. 5. The tailing effect is due to the surface tension and viscosity of the deposition fluidic. In our case, where DDT-AuNPs is used, the tailing effect is relatively long due to its low surface tension and low viscosity.

Figure 6(a) shows the nano-Au SRR (top) and microstrip (bottom) structures with a lattice size of 180 μm deposited on a 51 μm thick polyimide Kapton. Figure 6(b) shows individual images of the deposited SRRs and microstrips, and Fig. 6(c) illustrates the alternate stacking layers of SRRs and microstrip sheets. A maximum of three gold layers are deposited on the substrate, which limits the conductivity of the sample. However, increasing further the number of deposited layers would lead to smearing of the fluidic and degradation in structure resolution.

After deposition, the layer of DDT-AuNPs was annealed at 120–150 °C for 30 min to remove the dodecanethiol tail and form a thin shiny gold layer. The post annealed nano-Au surface roughness is found to be even [13] and has no significant scattering effects upon THz measurement. After the gold layer is annealed, a second substrate sheet is stacked on top of the deposited layers. The cleaned polymer substrate adheres well to the deposited layers below. The microstrips were deposited on the second

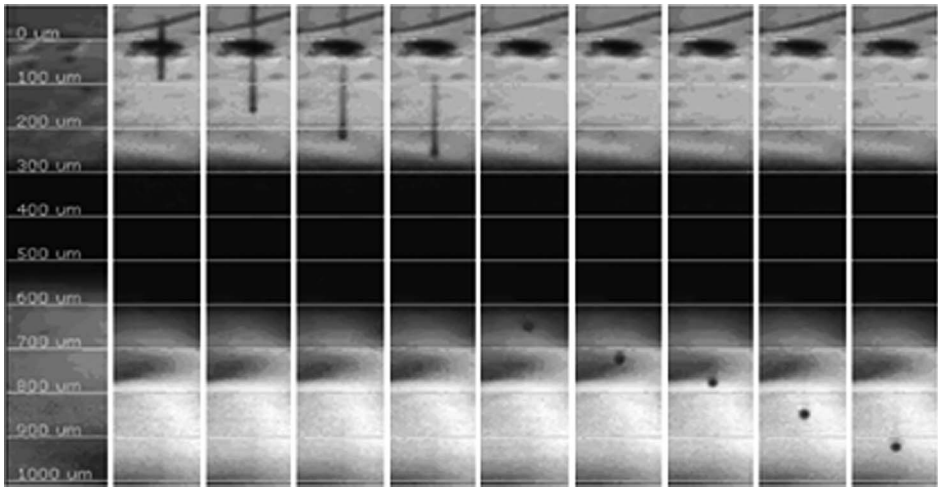

Fig. 5. Time of flight of DDT-AuNPs droplet jetting. Image taken by the system's built-in drop watcher camera. The relatively long "tailing" effect was due to its low surface tension and viscosity.

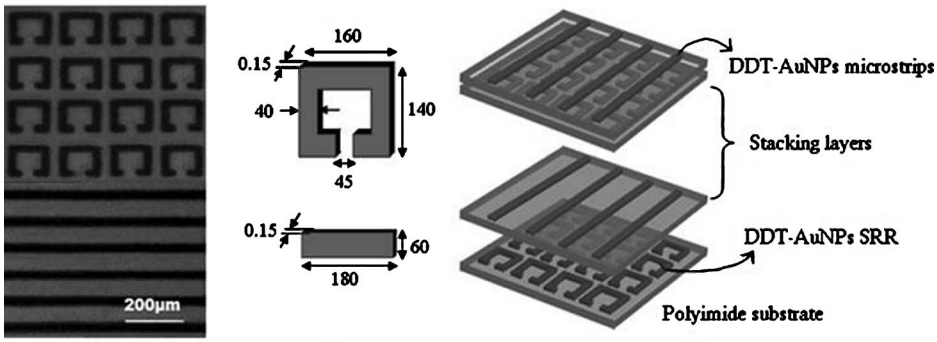

Fig. 6. (a) Fabricated result of SRR (up) and rod (down). (b) SRR and microstrip parameters in micrometers. (c) Illustration of stacking layers of 3D metamaterials.

substrate. The final fabrication product is up to six stacking sheets.

Since the sample cannot be removed from the deposited system until the end of the process, and the bottom layers are covered by the top layer, the thickness of the deposited nano-Au layer is difficult to measure using conventional equipment. Thus, the thickness t of one DDT-AuNPs layer is theoretically estimated by equating the volume of the deposited drop, $V_D = \pi t(d_D/2)^2$, and by determining drop volume, $V_j = (4\pi/3)(d_j/2)^3$, where d_D is the diameter of deposited drop on the substrate and d_j is the drop diameter obtained from the jetting image captured by the embedded camera of the fabrication system.

From the obtained data, the drop diameter is approximately $15 \pm 1\,\mu$m, while the drop volume is approximately 1.76 pl. The deposited drop diameter of DDT-AuNPs measured under a microscope is $30\,\mu$m. Since the captured image is not in high resolution, an uncertainty of $\pm 1\,\mu$m is estimated, which contributes $\sim 18\%$ of error. For a solid content of the DDT-AuNPs of 2% weight per volume, the remaining thickness of each deposited DDT-AuNPs layer is 49.65 nm after annealing. A maximum of three layers is deposited, which give a total thickness of $0.15\,\mu$m. Increasing the number of layers beyond three results in the spreading of the fluidic and degradation in the resolution of the SRR structure.

3. Characterization and Discussion

A T-ray 2000 spectroscopy system (Picometrix, Inc.) is used in the transmission mode [14,15] to characterize the samples. A sample is placed between the THz transmitter and the detector. The THz time-domain waveforms are acquired by recording the THz transmitted pulse at each sample orientation. Both the THz phase and amplitude as functions of frequency are acquired through a Fourier transform of the time-domain data. Absorbance is calculated from the time-domain measurements, which can be expressed as $a(v) = -\ln(T)$ where $T = (|E_T|/|E_o|)^2$ is the electric field transmission referenced to THz spectra with the sample removed. $|E_T|$ and $|E_o|$ are the magnitudes of the THz electric fields for the sample and the reference, respectively.

Figure 7 shows measured absorbance when the incident THz wave is normal to the sample plane. The sample is placed with the microstrips oriented at an angle of $\theta = 0°$, 30°, 60°, or 90° relative to the THz magnetic field. Note that $\theta = 0°$ corresponds to where the microstrips are parallel to the E field while $\theta = 90°$ corresponds to where the microstrips are perpendicular to the E field. This structure is shown to support frequency bands of 0.16, 0.53, and 0.76 THz for $\theta = 90°$ structure orientation. Since the magnetic field lies completely in the SRR plane, the measured electromagnetic responses are solely attributed to the electric resonant response of the structure [16]. For $\theta = 0°$, neither the E nor the H field from the incident wave drives the SRR; thus, the absorbance is featureless. However, for $\theta = 90°$, with the SRR in plane, the E field drives circulating current and leads to increments of the absorbance. Since there is no component of the H field propagating into the ring of the SRR, neither magnetic resonance nor bianisotropic response occurs; thus, the resonances are solely electric [17]. The measurements were repeated with the structure oriented at $\theta = 90°$ and then rotated from $\phi = 0°$ to 60°, where ϕ is the angle between the sample plane and the incident k vector.

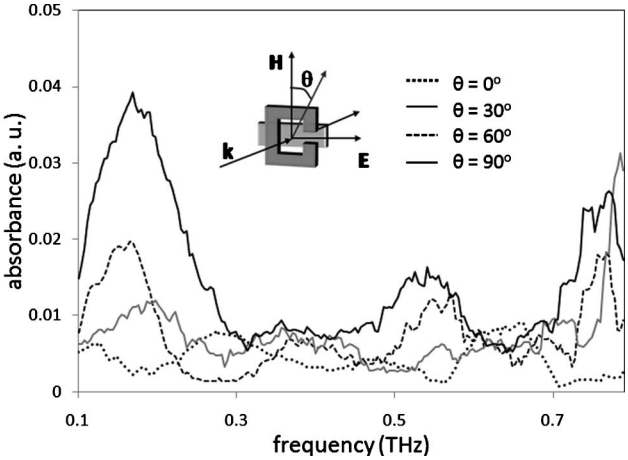

Fig. 7. Experimental result of 3D DDT-AuNPs with incident wave perpendicular to the sample plane. In the inset, the direction of the microstrips relative to the THz E field is indicated.

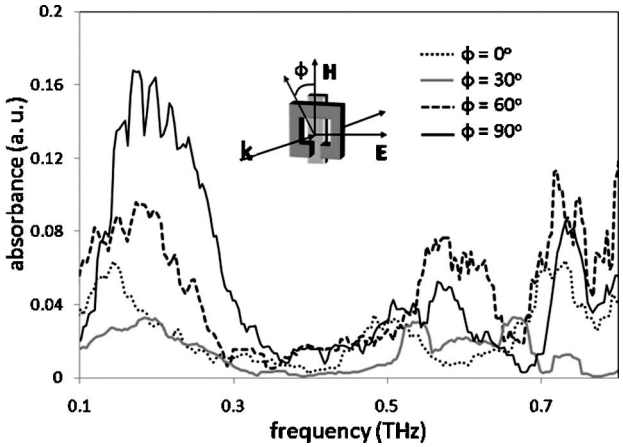

Fig. 8. Measured data of 3D DDT-AuNPs metamaterials with a variable angle of incidence (denoted by angle ϕ relative to the plane of the sample).

For this sample orientation, the THz magnetic field of the THz wave has a component perpendicular to the sample. Figure 8 shows the data obtained from the measurement. Note that, for $\phi = 0°$, the resonance occurs at the same frequencies as in the previous measurement data, of $\theta = 0°$ (see Fig. 7). For any ϕ angle with respect to sample plane, the electric resonance will be driven. With increasing the ϕ angle, the magnetic resonance will also be driven by a component of the H field along the axis of the SRR ring, where this encounters the bianisotropy effect. As the angle increases, the magnetic response of absorbance also increases due to the stronger H components. Also, Fabry–Perot interference due to the internal reflections between the stacking layers is obviously observed for large ϕ.

The calculation methodology of the effective parameters has been derived [18,19]. Using material parameters of DDT-Au nanoparticles, the fabricated metamaterial samples were simulated using the commercial software CST Microwave Studio. The calculated absorbance of the metamaterial is shown in Fig. 9. Because of resolution limitations in the microfluidic fabrication, the absorbance peak observed below 0.18 THz in Fig. 9 is relatively low compared to predictions. However, there is reasonable agreement between the data and the simulation.

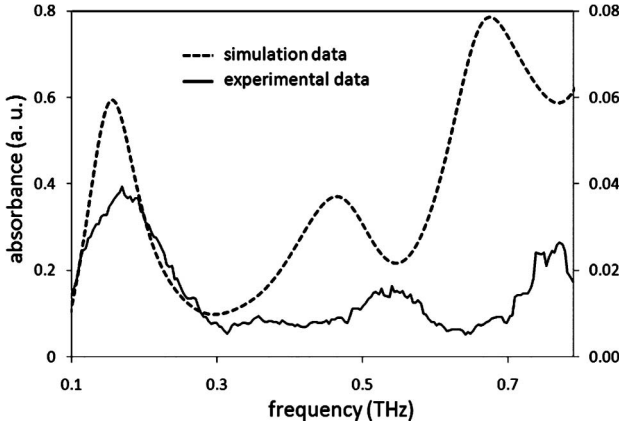

Fig. 9. Extract absorbance compared to measured absorbance.

4. Conclusion

The fabrication of flexible 3D DDT-AuNPs in the THz range is demonstrated. The structure size of 180 μm satisfies the effective medium theory condition that refractive effects dominate diffraction and scattering effects when the incident THz wavelength ranges from 3000 to 300 μm. The practice of stacking layers not only increases the conductivity of the sample, but also reduces the lattice length in the z direction, thereby making 3D metamaterials feasible. A maximum of three layers, with approximate thickness of 50 nm for each layer, are deposited, which limits the conductivity of the sample. Increasing the number of deposited layers leads to smearing of the fluidic and degradation in the accuracy of the SRR structure.

References

1. T. J. Yen, W. J. Padilla, N. Fang, D. C. Vier, D. R. Smith, J. B. Pendry, D. N. Basov, and X. Zhang, "Terahertz magnetic response from artificial materials," Science **303**, 1494 (2004).
2. W. J. Padilla, A. J. Taylor, C. Highstrete, M. Lee, and R. D. Averitt, "Dynamical electric and magnetic metamaterial response at terahertz frequencies," Phys. Rev. Lett. **96**, 107401 (2006).
3. B. G. Quan, X. L. Xu, H. F. Yang, X. X. Xia, Q. Wang, L. Wang, C. Z. Gu, and F. Li, "Time-resolved broadband analysis of split ring resonators in terahertz region," Appl. Phys. Lett. **89**, 041101 (2006).
4. H. O. Moser, B. D. F. Casse, O. Wilhelmi, and B. T. Saw, "Terahertz response of a microfabricated rod-split-ring-resonator electromagnetic metamaterials," Phys. Rev. Lett. **94**, 063901 (2005).
5. W. Wong, "Inkjet printer draws the line in manufacturing technology," Electronic Design **53**, 25 (2005).
6. J. C. Sturm, F. Pschenitzka, T. R. Hebner, M. H. Lu, and S. Troian, "Printing approaches for large-area color organic LED displays," Proc. SPIE **3797**, 266–274 (1999).
7. S.-C. Chang, J. Liu, J. Bharathan, Y. Yang, J. Onohara, and J. Kido, "Multicolor organic light emitting diodes processed by hybrid inkjet printing," Adv. Mater. **11**, 734–737 (1999).
8. F. Vitale, L. Mirenghi, E. Piscopiello, G. Pellegrini, E. Trave, G. Mattei, I. Fratoddi, M. V. Russo, L. Tapfer, and P. Mazzoldi, "Gold nanoclusters-organometallic polymer nanocomposites: synthesis and characterization," Mater. Sci. Eng. C **27**, 1300–1304 (2007).
9. D. Shalom, R. C. R. Wootton, R. F. Winkle, B. F. Cottam, R. Vilar, A. J. de Mello, and C. P. Wilde, "Synthesis of thiol functionalized gold nanoparticles using a continuous flow microfluidic reactor," Mater. Lett. **61**, 1146–1150 (2007).
10. I. Koltover, "Material matters—chemistry driving performance," Sigma Aldrich handbook 2, 3 (2007).
11. Y. L. Hor, "Terahertz response of microfluidic-jetted fabricated 3D flexible metamaterials," Ph.D. dissertation (New Jersey Institute of Technology, 2009).
12. C. Menzel, A. Bibl, and P. Hoisington, "MEMS solutions for precision micro-fluidic dispensing application," in *Imaging Science and Technology NIP 20: International Conference on Digital Printing Technologies* (Society for Imaging Science and Technology, 2004), Vol. 20, pp. 169–175.

13. J. Chung, S. Ko, C. P. Grigoropoulos, N. R. Bieri, C. Dockendorf, and D. Poulikakos, "Damage-free low temperature pulsed laser printing of gold nanoinks on polymers," J. Heat Transfer **127**, 724–732 (2005).
14. Y. L. Hor, J. F. Federici, and R. L. Wample, "Non-destructive evaluation of cork enclosures using terahertz/millimeter wave spectroscopy and imaging," Appl. Opt. **47**, 72–78 (2008).
15. Y. L. Hor, H. C. Lim, J. F. Federici, E. Moore, and J. W. Bozzelli, "Terahertz study of trichloroanisole by time-domain spectroscopy," Chem. Phys. **353**, 185–188 (2008).
16. R. Marques, F. Medina and R. Rafii-El-Idrissi, "Role of bianisotropy in negative permeability and left-hand metamaterials," Phys. Rev. B **65**, 144440 (2002).
17. H. Tao, A. C. Strikwerda, K. Fan, W. J. Padilla, X. Zhang, and R. D. Averitt, "Reconfigurable terahertz metamaterials," Phys. Rev. Lett. **103**, 147401 (2009).
18. C. R. Simovski, "Analytical modelling of double-negative composites," Metamaterials **2**, 169–185 (2008).
19. X. Chen, T. M. Grzegorczyk, B.-I. Wu, J. Pacheco, and J. A. Kong, "Robust method to retrieve the constitutive effective parameters of metamaterials," Phys. Rev. E **70**, 016608 (2004).